JOURNAL OF COMPUTATIONAL PHYSICS 62, 297–320 (1986)

A Mixed Pseudospectral/Finite Difference Method for the Axisymmetric Flow in a Heated, Rotating Spherical Shell

M. G. MACARAEG*

University of Tennessee Space Institute, Tullahoma, Tennessee 37388

Received September 4, 1984; revised January 30, 1985

A numerical solution technique for the axisymmetric flow in a differentially heated, rotating spherical annulus is developed. This method, based on the incompressible Navier–Stokes equations, simulates the Atmospheric General Circulation Experiment (AGCE) proposed for a future Shuttle mission. In the method a pseudospectral technique is used in the latitudinal direction, and a second-order accurate finite difference scheme discretizes time and radial derivatives. This pseudospectral/finite difference (PS/FD) method is applied to a hierarchy of cases of varying difficulty. The difficult cases are characterized by thinner Ekman layers resulting from higher rotation rates, larger difference in boundary temperatures, and stronger body forces. Comparison of the results establishes the higher accuracy and efficiency of the PS/FD method over the pure second-order accurate finite difference (FD) method. This paper discusses the development and performance of a mixed PS/FD model for the AGCE which has been modelled in the past only by pure FD formulations.

1. INTRODUCTION

The near zero gravity environment of the Shuttle presents the opportunity for the experimental simulation of the planetary atmosphere. A model experiment of the earth's atmospheric circulation, known as the Atmospheric General Circulation Experiment (AGCE), has been proposed for a later Spacelab flight [2]. The experiment will consist of concentric spheres rotating as a solid body as illustrated in Fig. 1. A dielectric fluid will be confined in a portion of the gap between the spheres by placing solid walls in the spherical domain. The annuus is subdivided to provide room for instrumentation. Temperature profiles on the spheres will simulate the equator to pole distribution and establish the large-scale vertical stability (warmer outer sphere) of the atmosphere. The gravitational body force on the atmosphere is simulated by application of an electric field across the gap which generates a radial body force in the dielectric fluid. It is the simulation of this force which requires the zero gravity environment of space, since the earth's gravitational force would greatly distort the simulated gravitational force field of the experiment.

* Present address: NASA Langley Research Center, Hampton, Virginia.

0021-9991/86 $3.00

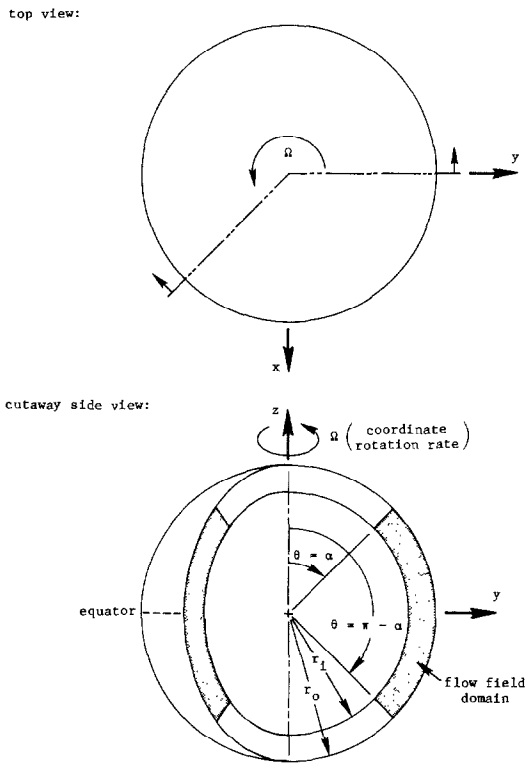

FIG. 1. Cutaway view of physical model.

A numerical model of the AGCE is needed to study the flow patterns as a function of varying experimental parameters such as rotation rates, thermal boundary conditions, or gravitational distribution across the gap. Finite difference models to determine the basic (axisymmetric) states have been developed [4, 12]. In those studies the effects of using a dielectric to simulate terrestrial gravity were, however, not addressed. Such effects are considered in [10].

Memory limitations imposed by the computing hardware (VAX 11/780) precluded an adequate check of the accuracy of the solutions produced by the finite difference FD models. However, spectral methods allow for much coarser grids and higher order accuracy so that resolution resuirements may be met and verified with the limited storage.

A hybrid scheme involving a pseudospectral latitudinal formulation and finite difference radial and time discretization was chosen for simplicity. However, as will be demonstrated, the finite difference discretization in the radial direction resolved the flow field on a coarser grid when coupled with the pseudospectral formulation as opposed to pure finite difference schemes.

In addition to the high accuracy one obtains with spectral methods, solutions

converged to a steady state (up to machine accuracy on a VAX 11/780) more quickly than the pure FD models. It was sufficient to use spectral methods in only one direction (latitude) and FD for the time and radial dependencies to achieve the above results.

Orszag and Israeli [17] and Orszag [16] applied a mixed spectral/finite difference scheme to the axisymmetric Stokes flow between concentric rotating spheres. The numerical model used a vorticity/stream function formulation. Taking advantage of the periodic flow, a modified Fourier series was used to expand the field variables. The present study retains the nonlinear advection terms in the Navier–Stokes equations coupled with the energy equation. The latitudinal dependence is expressed in terms of Tschebyshev polynomials as the latitudinal side walls (see Fig. 1) preclude the otherwise periodic flow in this direction. Other examples utilizing hybrid schemes can be found in Roache [21], Zang and Hussaini [25], or Reddy [19].

Merilees [11] made a series of numerical experiments to test the accuracy of the pseudospectral method. The tests were applied to the shallow water equations in spherical coordinates. The method was found to be more accurate than a fourth order FD scheme for the same resolution. However, questions concerning higher accuracy and efficiency (relative to a FD formulation) of spectral methods for coarser grids than the cases discussed in Merilees' model remained unanswered. Merilees' intent was to show the capability of pseudospectral methods and not to establish its advantages over finite difference schemes. Such questions will be addressed in the numerical study which follows.

In a spectral formulation the choice of expansion functions should be governed by the geometry of the problem as well as the ease and efficiency of implementation. Orszag and Israeli [18] have given some criteria on the type of functions to be used for different geometries. Both the spherical harmonics and Fourier series are optimal for periodic boundary conditions in the latitudinal direction. Efficient techniques using Fourier series applied to fluid-dynamical computations are given by Orszag [13]. However, the periodicity condition is violated in the AGCE due to the side walls. Depending on the final AGCE design these walls will be located at some latitudinal position. In the following numerical model these walls will be located at symmetric positions about the equator. This nonperiodicity in the latitudinal direction as well as the formation of boundary layers next to these side walls makes Tschebyshev polynomials a proper choice of expansion functions, since they allow for sharp boundary layer resolution and are applicable for nonperiodic conditions.

In this paper the equations governing the flow field of the AGCE are formulated followed by a development of the pseudospectral/finite difference scheme used in calculating the basic axisymmetric flow. Finally, selected results are presented to illustrate the advantages of the present approach.

Nomenclature

a	Coefficient of thermal expansion
A	Radial diffusion coefficient at $(i+1)$st mesh point
AGCE	Atmospheric General Circulation Experiment
B	Radial diffusion coefficient at ith mesh point
C	Radial diffusion coefficient at $(i-1)$st mesh point
Ek	Ekman number
FD	Finite difference
g	Gravitational acceleration (cm/s^2)
Gr	Grashof number
H	Re^{R^2}, where R is defined in Eq. (45)
k	Thermal conductivity ($cal/°C \cdot s$)
N	Upper truncation limit in Tschebyshev expansions
NR	Number of points in radial mesh
P	Pressure (dyn/cm^2)
PS	Pseudospectral
Pr	Prandlt number
r	Radial variable (cm)
r'	Nondimensional radius, r/r_0
r_i	Inner radius (cm)
r_0	Outer radius (cm)
T	Temperature (°C)
T'	Nondimensional temperature
T_0	Reference fluid temperature (°C)
u	Zonal (azimuthal) velocity (cm/s)
v	Latitudinal velocity (cm/s)
w	Radial velocity (cm/s)
z	Transformed θ variable for Tschebyshev polynomial domain
α	Angle location of latitudinal wall (radians)
γ	Parameter which determines degree of implicitness of radial diffusion terms
θ	Co-latitudinal angle measured from the z to y axis, or north to south (radians)
κ	Thermal diffusivity (cm^2/s)
ξ	Azimuthal component of vorticity $\times$ r sin θ (cm/s)
ξ'	Nondimensional ξ
ρ	Density of the fluid (g/cm^3)
ρ_0	Reference density of the fluid (g/cm^3)
ϕ	Azimuthal angle measured from the x to y axis, or west to east (radians)
ψ	Stokes' stream function (cm^3/s)
ψ'	Nondimensional stream function
ω	Azimuthal component of angular momentum per unit mass relative to the rotating frame
Ω	Solid body rotation rate (rad/s)

2. Formulation of Equations

The governing equations are given below in spherical polar coordinates (Fig. 2) which rotate with the apparatus at the constant angular velocity Ω about the z axis. Equations (1)–(3) are the momentum equations in the ϕ, θ, and r directions, respectively, Eq. (4) is the energy equation and Eq. 5 is the mass conservation equation. The ϕ (azimuthal), θ (latitudinal), and r (radial) components of velocities are given by u, v, and w, respectively. The exponent n, appearing in Eq. (3) is 0 for a uniform gravitational field, 2 for terrestrial gravity, or 5, which is appropriate for a dielectric force as used in the AGCE [7].

$$\frac{\partial u}{\partial t}+\frac{v}{r}\frac{\partial u}{\partial \theta}+w\frac{\partial u}{\partial r}+\frac{uw}{r}+\frac{uv\cot\theta}{r}$$

$$=-2\Omega(w\sin\theta+v\cos\theta)+\nu\left(\nabla^2 u-\frac{u}{r^2\sin^2\theta}\right) \tag{1}$$

$$\frac{\partial v}{\partial t}+\frac{v}{r}\frac{\partial v}{\partial \theta}+w\frac{\partial v}{\partial r}+\frac{vw}{r}-\frac{u^2\cot\theta}{r}$$

$$=\frac{-1}{r}\frac{\partial P}{\partial \theta}+2\Omega u\cos\theta+\nu\left(\nabla^2 v+\frac{2}{r^2}\frac{\partial w}{\partial \theta}-\frac{v}{r^2\sin^2\theta}\right) \tag{2}$$

$$\frac{\partial w}{\partial t}+\frac{v}{r}\frac{\partial w}{\partial \theta}+w\frac{\partial w}{\partial r}-\frac{1}{r}(u^2+v^2)$$

$$=\frac{-\partial P}{\partial r}+2\Omega u\sin\theta+\nu\left(\nabla^2 w-\frac{2w}{r^2}-\frac{2}{r^2\sin\theta}\frac{\partial v\sin\theta}{\partial \theta}\right)+\left(\frac{r_0}{r}\right)^n agT \tag{3}$$

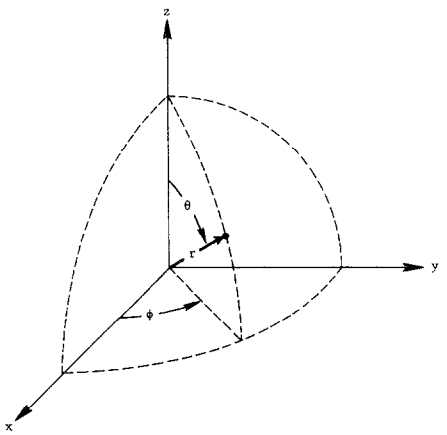

FIG. 2. The spherical coordinate system.

$$\frac{\partial T}{\partial t}+\frac{v}{r}\frac{\partial T}{\partial \theta}+w\frac{\partial T}{\partial r}=\kappa\nabla^2 T \tag{4}$$

$$\frac{1}{r^2}\frac{\partial}{\partial r}(r^2 w)+\frac{1}{r\sin\theta}\frac{\partial}{\partial\theta}(v\sin\theta)=0. \tag{5}$$

The equations are cast in a vorticity/stream function formulation with the new variables vorticity (ξ), stream function (ψ), and swirl (ω) defined below.

$$\xi = r\sin\theta(\nabla\times\bar{V})_\phi \tag{6}$$

$$w=\frac{1}{r^2\sin\theta}\frac{\partial\psi}{\partial\theta} \tag{7}$$

$$v=-\frac{1}{r\sin\theta}\frac{\partial\psi}{\partial r} \tag{8}$$

$$u=\frac{\omega}{r\sin\theta}. \tag{9}$$

The momentum and energy equations are nondimensionalized to facilitate comparison of results. The independent variables, r and t, are nondimensionalized by outer sphere radius and rotation rate, respectively. In nondimensionalizing temperature, the maximum temperature difference occurring on the latitudinal walls ($T_U - T_L$) was chosen. The characteristic radial velocity is taken as the solid body rotation rate (Ω) divided by the gap width ($r_0 - r_i$); all other length scales are nondimensionalized by the outer sphere radius (r_0). Nondimensional variables, denoted by primes, are given in Eqs. (10) through (14):

$$T=(T_U-T_L)T'+T_L \tag{10}$$

$$\xi = r_0\Omega\xi' \tag{11}$$

$$\psi=\psi' r_0^3\Omega \tag{12}$$

$$\omega=\omega' r_0^2\Omega \tag{13}$$

$$\bar{V}=\bar{V}' r_0\Omega_0. \tag{14}$$

When these equations are substituted into the dimensional equations ((1) through (5)) the nondimensional Grashof (Gr), Ekman (Ek), and Prandtl (Pr) numbers, defined in Eqs. (15) through (17), result:

$$\mathrm{Gr}=\frac{ga(T_U-T_L)\,r_0^3}{\nu^2} \tag{15}$$

$$\mathrm{Ek} = \frac{\nu}{r_0^2 \Omega_0} \tag{16}$$

$$\mathrm{Pr} = \frac{\nu}{\kappa}. \tag{17}$$

The nondimensional momentum and energy equations (where unprimed variables are here nondimensional) are

$$\frac{D\xi}{Dt} - \frac{2\xi}{r^3 \sin\theta}\left(\frac{\partial\psi}{\partial\theta} - r\cot\theta\frac{\partial\psi}{\partial r}\right) - \frac{2\omega}{r^3\sin\theta}\left(\frac{\partial\omega}{\partial\theta} - r\cot\theta\frac{\partial\omega}{\partial r}\right)$$
$$= \frac{2\Omega\sin\theta}{r}\left(\frac{\partial\omega}{\partial\theta} - r\cot\theta\frac{\partial\omega}{\partial r}\right) + \mathrm{Ek}\, D^2\xi + \mathrm{Gr}\,\mathrm{Ek}^2\sin\theta\left(\frac{1}{r}\right)^n\frac{\partial T}{\partial\theta} \tag{18}$$

$$\frac{D\omega}{Dt} = \frac{-2\Omega\sin\theta}{r}\left(\frac{\partial\psi}{\partial\theta} - r\cot\theta\frac{\partial\psi}{\partial r}\right) + \mathrm{Ek}\, D^2\omega \tag{19}$$

$$\frac{DT}{Dt} = \frac{\mathrm{Ek}}{\mathrm{Pr}}\nabla^2 T \tag{20}$$

$$D^2\psi = \xi, \tag{21}$$

where

$$D^2 = \frac{\partial^2}{\partial r^2} + \frac{\sin\theta}{r^2}\frac{\partial}{\partial\theta}\left(\frac{1}{\sin\theta}\frac{\partial}{\partial\theta}\right) \tag{22}$$

$$\frac{D}{Dt} = \frac{\partial}{\partial t} - \frac{1}{r^2\sin\theta}\left(\frac{\partial\psi}{\partial r}\frac{\partial}{\partial\theta} - \frac{\partial\psi}{\partial\theta}\frac{\partial}{\partial r}\right) \tag{23}$$

$$\nabla^2 = \frac{1}{r^2}\left(\frac{\partial}{\partial r}r^2\frac{\partial}{\partial r}\right) + \frac{1}{r^2\sin\theta}\frac{\partial}{\partial\theta}\left(\sin\theta\frac{\partial}{\partial\theta}\right). \tag{24}$$

The fluid is assumed to be incompressible except for the thermal expansion which produces a bouyancy. The density variation in the bouyancy term is represented by

$$\rho = \rho_0(1 - a(T - T_0)), \tag{25}$$

which is the classical Boussinesq approximation valid for flows with small density variations.

Boundary conditions appropriate for the AGCE as given in Eqs. (26) through (32) involve the no-slip condition and conducting walls. The numerical boundary condition for the vorticity is discussed in Section 3.

$$\psi\left(\frac{\pi}{4}, r\right) = \psi\left(3\frac{\pi}{4}, r\right) = 0 \qquad r_i \leqslant r \leqslant r_0 \tag{26}$$

$$\psi(\theta, r_i) = \psi(\theta, r_0) = 0 \qquad \pi/4 \leqslant \theta \leqslant 3\pi/4 \tag{27}$$

$$\omega\left(\frac{\pi}{4}, r\right) = \omega\left(3\frac{\pi}{4}, r\right) = 0 \qquad r_i \leqslant r \leqslant r_0 \tag{28}$$

$$\omega(\theta, r_i) = \omega(\theta, r_0) = 0 \qquad \pi/4 \leqslant \theta \leqslant 3\pi/4 \tag{29}$$

$$T\left(\frac{\pi}{4}, r\right) = T\left(3\frac{\pi}{4}, r\right) = mr - r_0 \qquad r_i \leqslant r \leqslant r_0 \tag{30}$$

$$m = \frac{T(\pi/4, r_0) - T(\pi/4, r_i)}{r_0 - r_i} \tag{31}$$

$$\begin{aligned} T(\theta, r_i) &= -\sin^2 2\theta \qquad && \pi/4 \leqslant \theta \leqslant 3\pi/4 \\ T(\theta, r_0) &= \cos^2 2\theta \qquad && \pi/4 \leqslant \theta \leqslant 3\pi/4. \end{aligned} \tag{32}$$

3. Solution Technique

The governing equations are approximated by a pseudospectral discretization for the latitudinal derivatives and a finite difference discretization for the radial and time derivatives. The θ domain is determined by the location of the latitudinal side walls at $\theta = \alpha$ and $\theta = \pi - \alpha$, which are therefore symmetric about an equator located at $\pi/2$ as was shown in Fig. 1. The pseudospectral development of the latitudinal dependence will be the initial focus of this section.

Pseudospectral Formulation

The typical Tschebyshev collocation points are $z_j = \cos[\pi_j/N]$ for $j = 0, 1, \ldots, N$. Since these points are clustered naturally near the endpoints of the domain, the boundary layers forming at the latitudinal walls are well resolved.

The physical domain $\alpha < \theta < \pi - \alpha$ is mapped onto the computational domain $-1 < z < 1$ with the transformation

$$z = \frac{2\theta - \pi}{\pi - 2\alpha}. \tag{33}$$

The Tschebyshev pseudospectral formulation for the latitudinal dependence of the model can be summarized as follows (vorticity is used for example):

1. Determine the initial conditions of the vorticity (ξ) flow field. Then, at each time step

2. Determine N coefficients $b_n(t)$ $(n = 0, 1, \ldots, N)$ so that

$$\xi(r, z_j, t) = \sum_{n=0}^{N} b_n T_n(z_j) \qquad 0 \leqslant j \leqslant N. \tag{34}$$

These coefficients are calculated by

$$b_n = \frac{2}{N\bar{c}_n} \sum_{p=0}^{N} \frac{1}{\bar{c}_p} \xi(z_p) \cos \frac{\pi p}{N} \qquad 0 \leqslant n \leqslant N, \tag{35}$$

where $c_0 = \bar{c}_N = 2$, and $c_n = 1$ for $0 < n < N$. These coefficients are needed only to evaluate derivatives since the pseudospectral technique involves solving the equations in physical space rather than in the spectral space with transforms used only to evaluate derivatives [14, 15].

3. Evaluate $\partial\xi/\partial z$ by differentiating Eq. (34):

$$\left(\frac{\partial \xi}{\partial z}\right)_j = \sum_{n=0}^{N} b_n T_n'(z_j) = \sum_{n=0}^{N} s_n T_n(z_j) \tag{36}$$

where

$$s_n = \frac{2}{\bar{c}_n} \sum_{p=n+1}^{N} p b_p \qquad \text{for} \quad p+n \text{ odd.} \tag{37}$$

In order to avoid N^2 operations to evaluate Eq. (36), the s_n may be obtained by a recursion formula [5]. Since differentiation involves a degree loss of the order of the Tschebyshev polynomial, s_N is set equal to 0. The remaining coefficients are obtained from the relations

$$\bar{c}_n s_n = s_{(n+2)} + 2(n+1)\, b_{(n+1)} \qquad n \leqslant N-2 \tag{38}$$

and $s_{(N-1)} = 2N b_N$.

Using Eq. (38), only $O(N)$ operations are needed to obtain s_n from b_n.

4. The second derivatives are obtained in a similar manner:

$$\left(\frac{\partial^2 \xi}{\partial z^2}\right)_j = \sum_{n=0}^{N} b_n T_n''(z_j) = \sum_{n=0}^{N} r_n T_n(z_j). \tag{39}$$

In this case the recursion formula given in Eq. (38) is used where the coefficients r_n are obtained from the first derivative coefficients:

$$\bar{c}_n r_n = r_{(n+2)} + 2(n+1)\, s_{(n+1)} \qquad n \leqslant N-2. \tag{40}$$

In evaluating the θ derivatives, a substantial gain in speed was obtained by setting up the matrix equivalent of the pseudospectral derivative formulation [6, 23, 26]. These matrices were set up outside of the time stepping process so that derivative evaluation involved only a simple matrix multiplication.

5. Finally, evaluate the unknowns in Eqs. (18) through (21) by solving, in physical space, at the collocation points, and proceed to the next time level.

Implementation of boundary conditions are the next consideration. Since the

coordinate system is rotating, all motion is relative to the solid body rotation rate Ω. Therefore the variable ω, which is proportional to the zonal velocity, is initially zero throughout the interior. For no-slip conditions all velocities are zero at the surrounding walls which implies that ω is zero at these walls. Since the solid walls are streamlines, any constant value of ψ may be selected; the conventional choice is to set ψ equal to zero. Temperature boundary conditions are fixed for all time since the model assumes conducting walls. A profile represented by $-\sin^2 2\theta$ is chosen at the inner sphere, and $\cos^2 2\theta$ at the outer sphere. Such a profile gives a stable radial temperature profile (warmer outer sphere) and unstable latitudinal distribution (temperature decreases from the equator to the pole). These trigonometric functions are chosen since symmetric conditions are automatically imposed about the equator. In addition, such a profile is similar to the conduction solution for a spherical shell. At the latitudinal walls, temperature is linearly interpolated between specified corner temperatures.

The vorticity boundary conditions are derived so that the no-slip conditions are satisfied. This is done by setting $\partial\psi/\partial\theta$ at the latitudinal walls equal to zero. From Eq. (6),

$$\xi_{\text{wall}} = -\sin\theta\left(r\frac{\partial v}{\partial r} + v - \frac{\partial w}{\partial\theta}\right)_{\text{wall}} = \left(\sin\theta\frac{\partial w}{\partial\theta}\right)_{\text{wall}}. \tag{41}$$

Recalling that

$$w = \frac{1}{r^2\sin\theta}\frac{\partial\psi}{\partial\theta} \tag{42}$$

so that

$$\left.\frac{\partial w}{\partial\theta}\right|_{\text{wall}} = \left(\frac{1}{r^2}\frac{-\cos\theta}{\sin^2\theta}\frac{\partial\psi}{\partial\theta} + \frac{1}{r^2\sin\theta}\frac{\partial^2\psi}{\partial\theta^2}\right)_{\text{wall}} = \left(\frac{1}{r^2\sin\theta}\frac{\partial^2\psi}{\partial\theta^2}\right)_{\text{wall}} \tag{43}$$

we therefore obtain

$$\xi_{\text{wall}} = \left.\frac{1}{r^2}\frac{\partial^2\psi}{\partial\theta^2}\right|_{\text{wall}}. \tag{44}$$

Since in a spectral formulation second derivatives are linear combinations of first derivatives, the no-slip condition is applied by calculating the second derivative of the stream function, given in Eq. (44), from a first derivative field having zero values at the boundaries.

The flow field variables are either symmetric or antisymmetric about the equator at $\pi/2$ since latitudinal walls are located at $\pi/4$ and $3\pi/4$ in this study. Therefore, flow field variables need only be calculated for half the domain if the symmetries are imposed.

Finite Difference Formulation

In the radial direction, high resolution is needed near the spherical boundaries where Ekman layer (boundary layers near the curved surfaces) formation occurs. The physical domain $r_i \leqslant r \leqslant r_0$ is therefore mapped onto the computational domain $-e \leqslant H \leqslant e$, where H is defined in Eq. (45). Several exponential or logarithmic functions would serve as a satisfactory choice for H [22] since the function must increase linearly in the interior and much more rapidly near the endpoints. The function given below gave a distribution of points which resolved the Ekman layers in this study:

$$H(r) = \mathrm{Re}^{R^2} \qquad \text{where} \quad R = \frac{2r - r_i - r_0}{r_0 - r_i}. \tag{45}$$

As discussed in the pseudospectral formulation, the stream function and swirl are zero at the solid walls, and the temperature profile is proportional to $-\sin^2(2\theta)$ at the inner sphere and $\cos^2(2\theta)$ at the outer sphere. For proper application of the no-slip condition, vorticity values at the boundary must incorporate this assumption. Williams [24] derived a vorticity boundary condition, consistent with a second-order accurate scheme, which is given in Eq. (51). This condition is sometimes referred to as Jensen's condition [20]. If the radial wall position is denoted as grid point one and the variable n denotes grid points in the latitude, the boundary condition for vorticity is

$$\begin{aligned}
\xi(n, 1) &= \frac{1}{r^2} \frac{\partial^2 \psi}{\partial r^2}\bigg|_{\text{wall}} \\
&= \frac{1}{\Delta r^2}\left[3.5\psi(n, 1) + 0.5\psi(n, 3) - 4\psi(n, 2) + 3\Delta r \left(\frac{\partial \psi}{\partial r}\right)_{\text{wall}}\right] + O(\Delta r)^2 \\
&= \frac{1}{\Delta r^2}\left[3.5\psi(n, 1) + 0.5\psi(n, 3) - 4\psi(n, 2)\right] + O(\Delta r)^2.
\end{aligned} \tag{46}$$

In this way the no-slip boundary condition is allowed to diffuse into the overall system.

Poisson Solution for Stream Function

The Poisson equation for stream function was solved in two ways. Initially a pseudo-time derivative was introduced so that at steady state the Poisson equation would be satisfied. During this internal iteration, latitudinal derivatives were not updated. In other words, the following equation was solved:

$$\frac{\partial^2 \psi}{\partial r^2} = f \tag{47}$$

where

$$f=\frac{\sin\theta}{r^2}\frac{\partial}{\partial\theta}\left(\frac{1}{\sin\theta}\frac{\partial\psi}{\partial\theta}\right)+\xi. \tag{48}$$

Representing the pseudo-time parameter as τ and the global time iteration as t, Eqs. (47) and (48) are therefore

$$\frac{\Psi^{\tau+\delta\tau}-\Psi^{\tau}}{\delta\tau}=\left(\frac{\partial^2\psi^{\tau+\delta\tau/2}}{\partial r^2}\right)^t-\frac{\sin\theta}{r^2}\frac{\partial}{\partial\theta}\left(\frac{1}{\sin\theta}\frac{\partial\psi}{\partial\theta}\right)^t+(\xi)^{t+\delta t}. \tag{49}$$

Alternatively, the matrix corresponding to the Laplacian operator was inverted by a conventional LU decomposition and back solution.

The former technique allowed an order of magnitude larger global time step (δt) to be used in the global iteration as compared to when the direct Poisson solver was used. Since the ψ field evolved more slowly due to the non-updated latitudinal derivatives, however, more global iterations were required.

Time Discretization

For convenience the equation form may be written as

$$\frac{\partial f}{\partial t}=\mathrm{NLT}+\Phi T+\nu D^2 f. \tag{50}$$

These equations are solved uncoupled but implicitly in terms of the radial diffusion terms. The nonlinear terms (NLT), rotation terms (ΩT), and spectral diffusion terms (latitudinal derivatives in $\nu D^2 f$) are handled explicitly. The rotation and nonlinear advection terms utilize updated values of stream function to evaluate derivatives which were found to relax the time interval restriction considerably, as one would expect. Although the spectral diffusion terms were handled explicity the stringent time step restriction associated with a Tschebyshev mesh was not severe since the mesh was fairly coarse.

The equations are written in tridiagonal form with respect to the radial derivatives. The swirl equation will be used to show the equation format. Again, n denotes a given θ position and i denotes radial points:

$$\begin{aligned}\frac{1}{\delta t}\omega_{n,i}^{t+\delta t}-\gamma[A_i\omega_{n,i+1}+B_i\omega_{n,i}+C_i\omega_{n,i-1}]^{t+\delta t}\\ =\frac{1}{\delta t}\omega_{n,i}^{t}+(1-\gamma)[A_i\omega_{n,i+1}+B_i\omega_{n,i}+C_i\omega_{n,i-1}]^{t}\\ +\mathrm{NLT}^t+\Omega\mathrm{T}^t+(\theta\text{ viscous terms})^t.\end{aligned} \tag{51}$$

4. Model Verification

Diagnostics

To determine whether the flow field was accurately resolved a case representative of the AGCE was selected, having an acceleration due to gravity equal to 980 cm/s^2 and a solid body rotation rate of 1 rad/s. The fluid was silicone oil (properties are listed in Table I). The inner and outer sphere radii were set equal to 5 and 6 cm, respectively. This case was calculated at three resolutions, 8×12, 16×12, and 32×12, where the first number refers to the number of mesh points in the latitude from $\pi/4$ to $\pi/2$, and the second number is the number of mesh points in the radial direction. To assess the agreement between the different resolutions a difference norm was calculated at matching latitudinal points. The difference norm should decrease as resolutions are increased which would indicate that the flow field was better resolved as grids became finer. The difference norm is defined in the following equation, where F is a given flow field variable; subscripts 1 and 2 signify different resolutions, and NR refers to the number of radial points. $F_{\max}$ is the maximum value of the flow field quantity for the higher resolution mesh.

$$\text{difference norm} = \frac{[\sum_{n=1}^{N} \sum_{i=1}^{\mathrm{NR}} (F_1(n, i) - F_2(n, i))^2]^{0.5}}{N \times F_{\max}} \tag{52}$$

Difference norms for the 8×12 and 16×12 resolutions were on the order of 10^{-3}, and 10^{-6} to 10^{-7} for the 16×12 and the 32×12 resolutions, which indicates that the 16×12 mesh is as accurate as the 32×12 mesh. Difference norm calculations are given in Table II.

A mass and heat balance over the flow field domain was also used to verify the model. Since there are no sources or sinks in the model and the flow is steady, the amount of heat entering the domain must equal the amount escaping. These heat fluxes described by Fourier's law were calculated by integrating along the boundary. Figure 3 identifies the parameters and direction of heat flow assumed. A mass balance was evaluated at all points in the flow field. For this diagnostic velocities in the conservation of mass equation were nondimensionalized by maximum velocities in the flow field.

TABLE I

Silicone Oil Properties

Property	Value
Kinematic viscosity (ν)	10^{-2} cm^2 s^{-1}
Thermal diffusivity (κ)	5.96×10^{-4} cm^2 s^{-1}
Expansivity (a)	1.34×10^{-3} °C^{-1}
Prandtl number (Pr)	16.8

TABLE II

Difference Norm Calculations

Resolutions compared	ξ	ψ	ω	T
8×12, 16×12	3.29×10^{-3}	2.05×10^{-3}	3.79×10^{-3}	2.33×10^{-3}
16×12, 32×12	1.83×10^{-6}	4.12×10^{-7}	7.52×10^{-7}	7.84×10^{-7}

Periodic calculations during the time iteration process were made to ascertain the amount of change occurring between two succeeding time steps. These residuals are defined by

$$(\text{residual of } F)^{t+\delta t} = \frac{F^{t+\delta t} - F^t}{F^{t+\delta t}} \tag{53}$$

and substantiated that the solution was converging.

Convergence Criteria

Criteria established to etermine when a steady state solution had been achieved involved the diagnostic tests just discussed. The following conditions were required to establish adequate convergence:

1. The ratio of the amount of heat entering the flow field domain over that leaving, subtracted from one, was within 5% of zero.

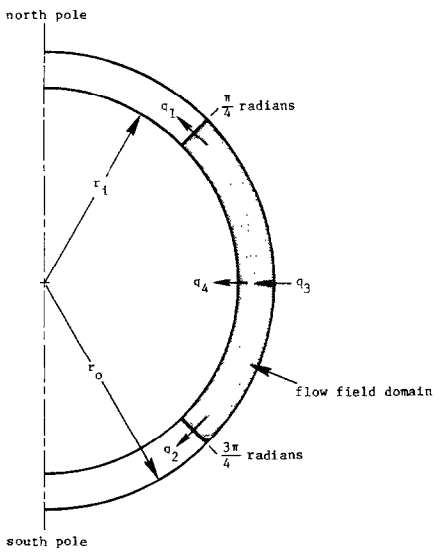

FIG. 3. Heat balance diagram.

2. The conservation of mass equation was satisfied, after normalization, to within 10^{-4} and 10^{-5} of zero.

3. Residuals calculated from Eq. (53) were on the order of 10^{-6} to 10^{-7} (machine zero), and persisted for at least 100 s (approximately 2000 iterations).

Test Cases

Closed-form solutions for the system of equations ((18) through (21)) of this study are not possible. In lieu of an analytical solution, an existing finite difference numerical solution for the same geometrical configuration was used for validation purposes [4]. This numerical solution is a pure FD model of the AGCE which was written in a general format to accommodate cylindrical as well as spherical geometries. The finite difference code has been verified with experimental data from a rotating, differentially heated cylindrical annulus, as well as against spherical spin-up data, results of which are to be published [9]. (Spin-up is the process by which a fluid adjusts to a change in the magnitude of the rotation rate of its container.)

Four test cases were set up with the Ekman layer being made harder to resolve in each succeeding case. The temperature distribution on the outer sphere was chosen to be equal to $\cos^2 2\theta$, and at the inner sphere $-\sin^2 2\theta$. Temperatures on the side walls were taken to be linear. The side walls were located at $\pi/4$ and $3\pi/4$ radians (symmetric about the equator). A schematic of this set-up is given in Fig. 3.

TABLE III

Test Cases

Model	Resolution ($\theta \times r$)	CPU time (min)	δt (s)	Number of iterations
	A. Case I: $g = 0.980$ cm/s^2, $\Omega = 0.001$ rad/s			
FD	30×20	5.5		200
PS/FD ($\gamma = 0.5$)	8×10	5.2	0.05	1000
	B. Case II: $g = 9.80$ cm/s^2, $\Omega = 0.01$ rad/s			
FD	30×20	14.0		500
PS/FD ($\gamma = 0.5$)	8×10	5.2	0.05	1000
	C. Case III: $g = 98.0$ cm/s^2, $\Omega = 0.10$ rad/s			
FD	30×20	30.0		1000
PS/FD ($\gamma = 0.5$)	8×12	22.0	0.05	3000
	D. Case IV: $g = 980.0$ cm/s^2, $\Omega = 1.0$ rad/s			
FD	30×20	90.0		4000
PS/FD ($\gamma = 0.5$)	16×12	98.4	0.03	6000
PS/FD ($\gamma = 1.0$)	16×12	82.2	0.05	5000

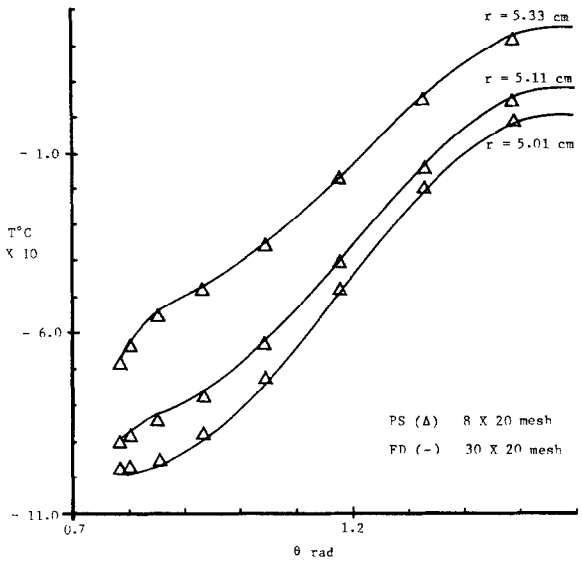

FIG. 4. Case II: T vs θ.

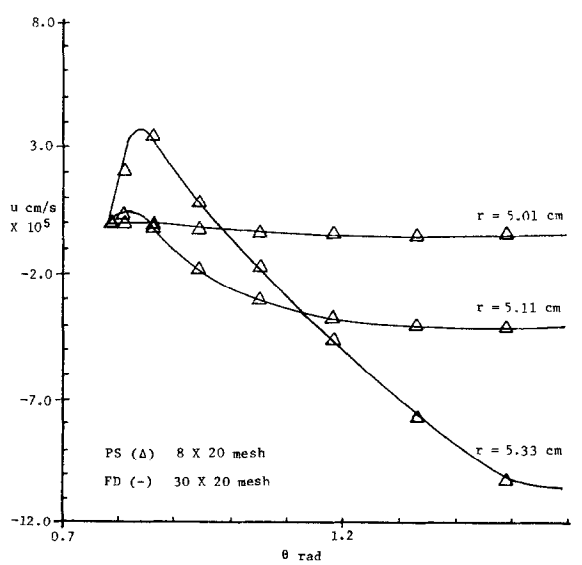

FIG. 5. Case II: u vs θ.

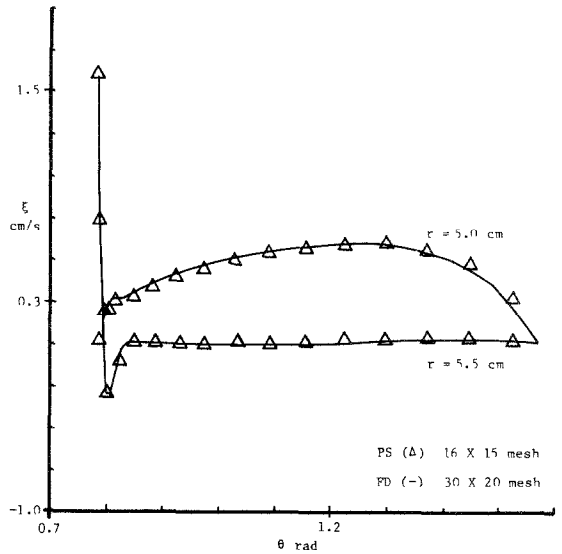

FIG. 6. Case IV: ξ vs θ.

The four test cases differed in rotation rates and gravitational acceleration as indicated in Table III. Different resolutions ranging from a 12×8 (12 points in the latitude measured from $\pi/4$ to $\pi/2$) to a 30×20 grid were run by the finite difference model. The finite difference model ran these cases at three resolutions: 8×12, 16×12, and 30×20 (where the first dimension refers to points in the latitude, from $\pi/4$ to $\pi/2$). A comparison of the solutions obtained on the 16×12 mesh and 30×20 mesh showed that the coarse grid solution did not resolve the flow field.

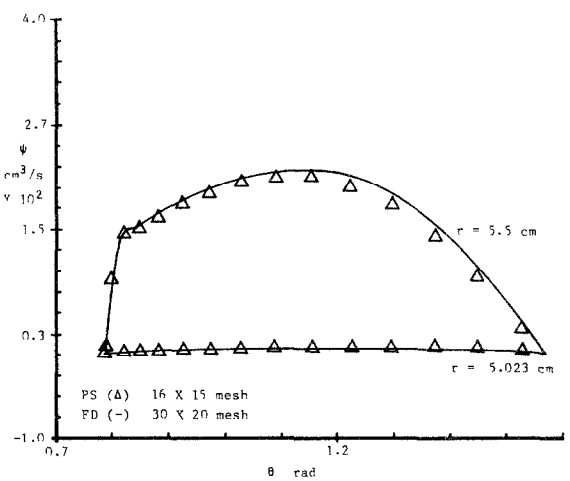

FIG. 7. Case IV: ψ vs θ.

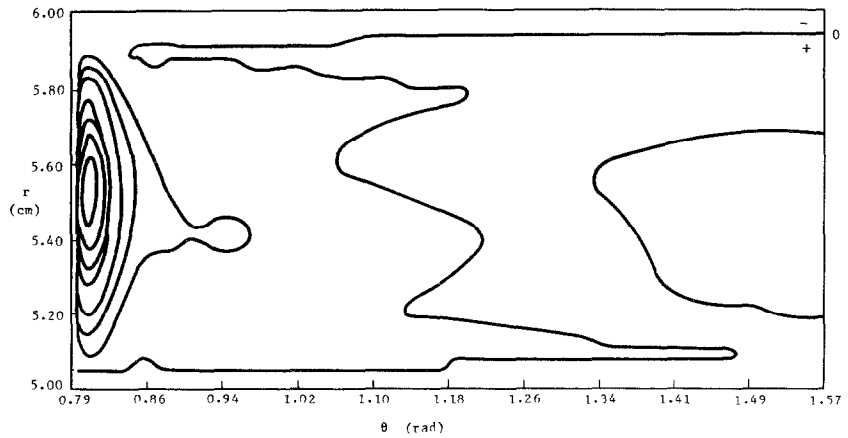

FIG. 8. Case II: Radial velocity contour plot (contour increment $= 1.5 \times 10^{-3}$), FD Model (12×8).

With the pseudospectral formulation only eight points in the latitude for Cases I through III were required. For Case IV the pseudospectral formulation required a 16×12 mesh to resolve the gradients in the boundary layer. These results are summarized in Table III. Also appearing in Table III are respective CPU times for each model to reach convergence. These values should not be regarded as conclusive evidence of a PS/FD formulation reaching convergence more quickly than a pure FD code since differences exist between their basic formulation. The FD code, written in primitive variable form, utilized a variable time step in its iteration scheme in a fully implicit algorithm. The PS/FD model only handled radial diffusion implicity and no attempt was made to vary the time step as iterations proceeded. What should be noted are that the much coarser grids allowable in the PS/FD code,

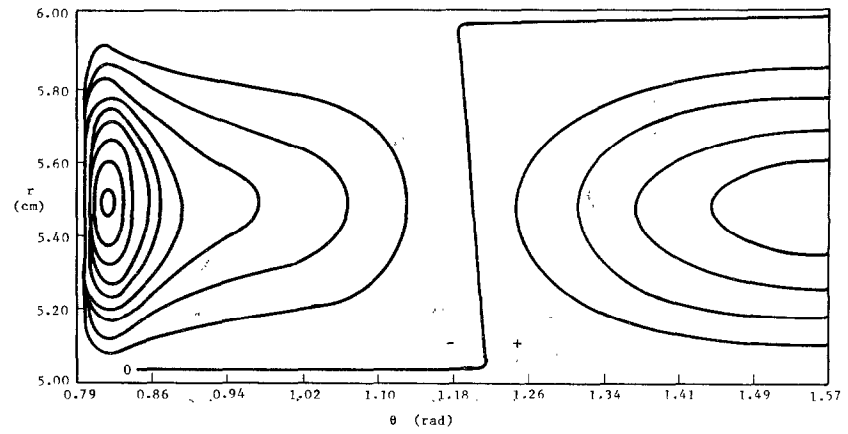

FIG. 9. Case II: Radial velocity contour plot (contour increment $= 1.5 \times 10^{-4}$), FD Model (30×20).

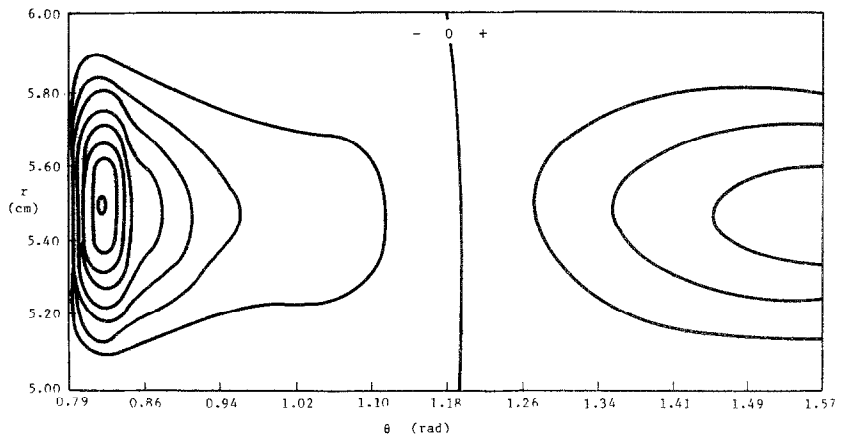

FIG. 10. Case II: Radial velocity contour plot (contour increment $= 1.5 \times 10^{-4}$). PS/FD Model (8×10).

relative to the finer grids required in the pure FD formulation to attain comparable accuracy, allowed the present method to be competitive in machine time.

A parameter γ, which represents the degree of implicitness of the radial diffusion terms (see Eq. (51)), was set equal to 0.5 (Crank–Nicolson) for Cases I through III. For Case IV it was found that setting $\gamma = 1.0$ allowed a time interval increase from 0.03 to 0.05 and a subsequent decrease in CPU time of 17% (see Table III). This is expected since setting $\gamma = 1$ is equivalent to a backward Euler scheme which is unconditionally stable thus allowing an arbitrarily large time step. Though $\gamma = 0.5$ is also unconditionally stable a large time step will cause some Fourier modes to overshoot [20].

A quantitative comparison between the two models was carried out by plotting flow field variables (ξ, ψ, T, and u) against radial positions for given latitudes and against latitudinal points for given radial positions. For ease of viewing the comparison, the PS/FD model is represented by discrete points and the FD model by a continuous line, since the latter has a greater number of points in its computational mesh. At least two positions were chosen per plot, one near the boudary and the other slightly beyond this point where a given profile seemed to change significantly. It was not possible in all cases to obtain comparable radial (or latitudinal) points for plotting all theta (or radial) positions since the two models utilized different nonuniform grids. A cubic spline interpolation was applied to the PS/FD model's data to obtain comparable radial points with the FD model. To generate comparable latitudinal points the Tschebyshev expansion coefficients were used. Comparisons of T, ψ, ξ, and u versus r for a given θ position showed agreement was very good. Representative plots from Cases II and IV are given in Figs. 4 through 7. Recall that Case II utilized only 8 points in the latitude as opposed to 30 points used in the FD formulation, and Case IV, which had the thinnest boundary layers, utilized 16 points in the latitude as opposed to the 30 points needed in the FD

model. Figures 4 and 5 are plots of temperature and zonal velocity, respectively, taken from Case II. Agreement is nearly exact to plotting accuracy. Plots of vorticity and stream function shown in Figs. 6 and 7 are taken from Case IV. Slight discrepancies are noted as would be expected from model differences.

The test cases run by both the FD and PS/FD model revealed some interesting observations regarding a PS formulation, the methodology in the latitude. In all four cases a much coarser grid was allowed in the PS/FD model (see Table III). To obtain adequate resolution the finite difference model required more than a 16×12 mesh. The PS/FD model utilized an 8×10 mesh in Cases I and II, 8×12 for Case III, and 16×12 for Case IV. The coarser grid allowable in the radial direction shows that a gain in accuracy for a coarser mesh will be obtained when a finite difference scheme is coupled with a pseudospectral formulation.

To illustrate the different resolution requirements for each model, radial velocity contour plots are given in Figs. 8 through 10 for Case II. The abscissa is incremented from the wall at $\pi/4$ to the equator. The FD model was unable to resolve this case on a 12×8 mesh, whereas the PS formulation gave excellent resolution utilizing an 8×10 mesh. Figure 8 shows the FD model results for a 12×8 mesh (recall that the first dimension refers to points in the latitudinal domain). Comparing these results with results in Fig. 9 for a 30×20 finite difference mesh, shows the need for the higher resolution. Comparison of the results for the pseudospectral 8×10 mesh is shown in Fig. 10. With roughly one-fourth the number of grid points in the latitude, the contours indicate that the pseudospectral results are comparable to the 30×20 FD mesh.

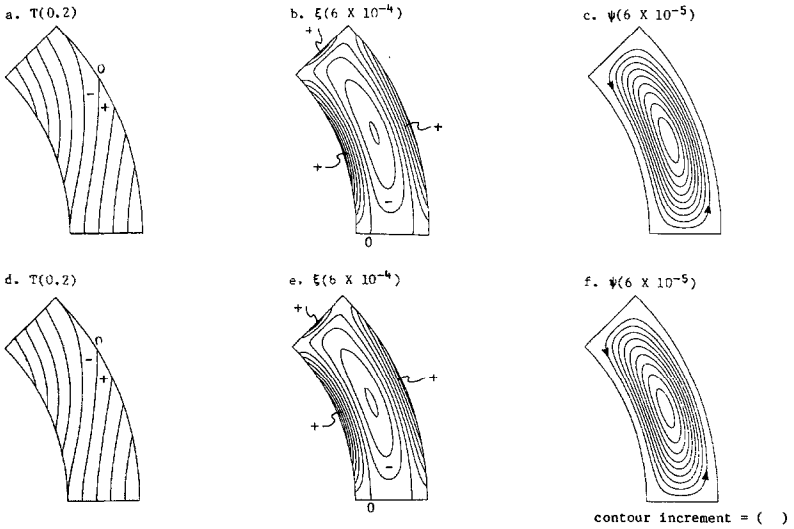

FIG. 11. Case I: Comparative contour plots of T, ξ, and ψ. (a, b, c) Contours of T, ξ, and ψ calculated from FD model using a 30×20 mesh. (d, e, f) Contours of T, ξ, and ψ calculated from PS/FD model using an 8×10 mesh.

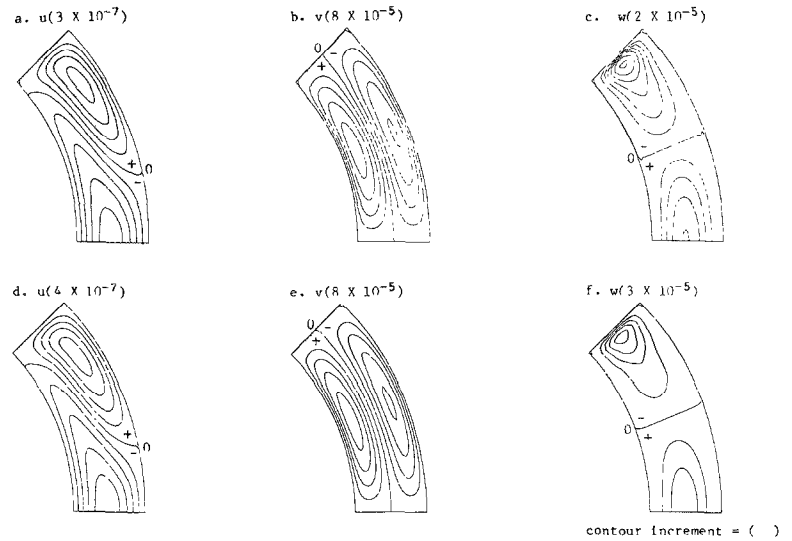

FIG. 12. Case I: Comparative contour plots of velocities. (a, b, c) Contours of u, v, and w calculated from FD model using 30×20 mesh. (d, e, f) Contours of u, v, and w calculated from PS/FD model using an 8×10 mesh.

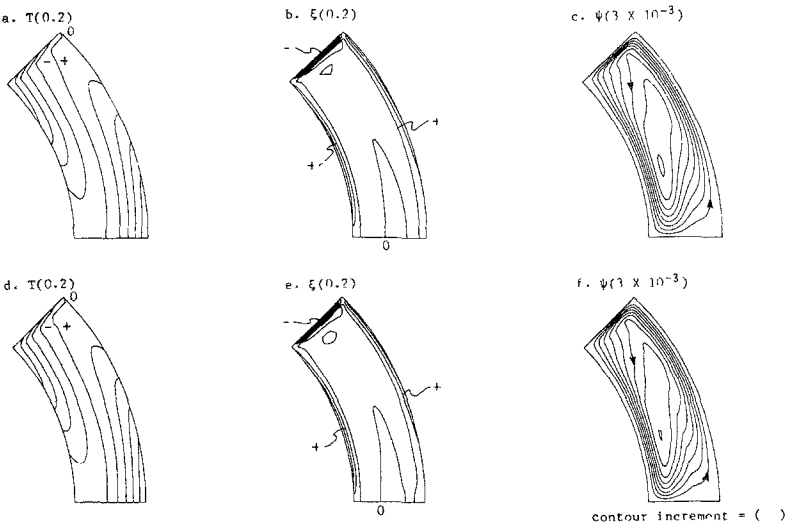

FIG. 13. Case IV: Comparative contour plots of T, ξ, and ψ. (a, b, c) Contours of T, ξ, and ψ calculated from FD model using a 30×20 mesh. (d, e, f) Contours of T, ξ, and ψ calculated from PS/FD model using a 16×12 mesh.

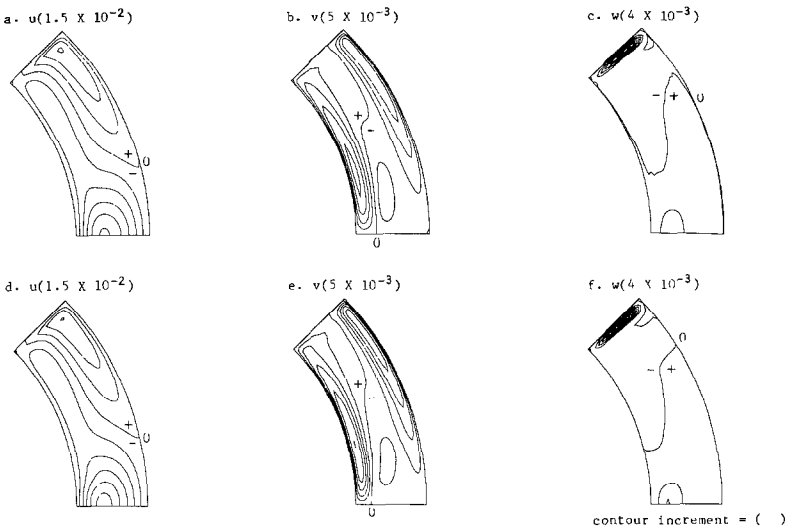

FIG. 14. Case IV: Comparative contour plots of velocities. (a, b, c) Contours of u, v, and w calculated from FD model using a 30×20 mesh. (d, e, f) Contours of u, v, and w calculated from PS/FD model using a 16×12 mesh.

Figures 11 through 14 are the contour plots corresponding to Cases I and IV described in Table III. The cross sections shown represents the portion of the gap extending from the wall at $\pi/4$ to the equator. Since symmetry (T, u, ω) or asymmetry (ψ, ξ, v) is imposed about the equator, only half of the domain is shown. Figures 11 and 12 pertain to Case I. Figures 11a, b, and c, are contour plots of temperature, vorticity, and stream function calculated by the FD model with a 30×20 mesh. Figures 11d, e, and f are the corresponding contour plots from the pseudospectral model on an 8×10 mesh. Figures 12a, b, and c are the FD contours of zonal, latitudinal, and radial velocities on a 30×20 mesh, followed by the same velocities (Figs.12d, e, and f) calculated by the PS/FD model. Similarly Figs. 13 to 14 apply to Case IV. In all cases the pseudospectral formulation required roughly one-fourth the number of points except for Case IV where 16 points were required in the latitude as opposed to the 30 points used in the FD model.

5. CONCLUSIONS

The preceding study concerned the development of a PS/FD model and its subsequent application to physical cases relevant to the Atmospheric General Circulation Experiment. A pseudospectral formulation was used in the latitude and finite difference discretized time and radial dependencies. It was found that roughly

one-seventh to one-third the number of points were needed in the PS/FD model, as opposed to a pure FD model of AGCE.

Pseudospectral derivatives were obtained using a matrix multiplication which

number of points needed in this study. The coarse grid and matrix formulation used in the PS/FD model allowed converged solutions to be obtained in machine times competitive with the FD model.

In addition to the matrix formulation for spectral derivatives efficiency gains were also due to the following considerations. Time step restrictions were substantially relaxed by updating derivatives of stream function in the advection and rotation terms prior to their usage in the temperature and swirl equations. Non-updated latitudinal derivatives for the pseudo-time iteration in the Poisson equation resulted in a further increase in the allowable time step.

It was shown that coupling the finite difference discretization with a spectral technique enabled the use of a coarser grid in both spatial directions. Thus the finite difference scheme performed more efficienctly in this context relative to a pure finite difference formulation.

REFERENCES

1. J. W. COOLEY AND J. W. TUKEY, *Math. Comput.* **19** (1965), 297.
2. W. W. FOWLIS AND G. H. FICHTL, *in* "Proceedings, Third NASA Weather and Climate Program Science Review," NASA Conf. Publ. 2029, Paper No. 32, p. 177, 1977.
3. W. W. FOWLIS AND R. HIDE, *J. Atmos. Sci.* **22** (1965), 541.
4. W. W. FOWLIS AND G. O. ROBERTS, The numerical design of a spherical baroclinic experiment for Spacelab flights, *in* "Proceedings, International Conference on Computational Methods and Experimental Measurement," Washington, D.C., 1982.
5. D. GOTTLIEB AND S. A. ORSZAG, "Numerical Analysis of Spectral Methods: Theory and Applications," Soc. Indus. Appl. Math., Philadelphia, 1977.
6. D. GOTTLIEB, S. A. ORSZAG, AND E. TURKEL, *Math. Comput.* **37** (1981), 293.
7. J. E. HART, "Studies of Earth Simulation Experiments," NASA Contractor Report NASA CR-2753, 1976.
8. M. Y. HUSSAINI, C. L. STREET, AND T. A. ZANG, "Spectral Methods for Partial Differential Equations," Conference on Applied Mathematics and Computing ARO Report 84-1, 1984.
9. F. W. LESLIE, Spherical spin-up experiments with numerical verification, NASA Marshall Space Flight Center, Huntsville, 1983, to be published.
10. M. G. MACARAEG, "Numerical Model of the Axisymmetric Flow in a Heated, Rotating Spherical Shell," Ph. D. dissertation, University of Tennessee Space Institute, 1984.
11. P. E. MERLIEES, *Atmosphere* **12** (1974), 77.
12. T. L. MILLER AND R. L. GALL, *J. Atmos. Sci.* **40** (1983).
13. S. A. ORSZAG, *Phys. Fluids (Suppl. 2)* **12** (1969), 250.
14. S. A. ORSZAG, *Stud. Appl. Math.* **50** (1971), 253.
15. S. A. ORSZAG, *J. Fluid Mech.* **50** (1971), 689.
16. ORSZAG, *Mon. Weather Rev.* **102** (1974), 56.
17. S. A. ORSZAG AND M. ISRAELI, *in* "Proceedings, Symposium on Numerical Models of Ocean Circulations," National Academy of Sciences, Washington, D. C., p. 284, 1972.
18. S. A. ORSZAG AND M. ISRAELI, *Annu. Rev. Fluid Mech.* **6** (1974), 281.

19. K. C. REDDY, *AIAA J.* **21** (1983), 1208.
20. P. C. ROACHE, "Computational Fluid Dynamics," Hermosa, Albuquerque, 1972.
21. P. C. ROACHE, *J. Comput. Phys.* **27** (1978), 204.
22. G. O. ROBERTS, *in* "Proceedings, 2nd International Conference on Numerical Methods in Fluid Dynamics," Vol. 8, p. 171, 1971.
23. T. D. TAYLOR, R. S. HIRSCH, AND M. NADWORNY, *J. Comput. Phys.* **12** (1984), 1.
24. G. P. WILLIAMS, *J. Atmos. Sci.* **24** (1967), 144.
25. T. A. ZANG, AND M. Y. HUSSAINI, *in* "Proceedings, 7th International Conference on Numerical Methods in Fluid Dynamics," Vol. 10, p. 461, 1981.
26. T. A. ZANG AND M. Y. HUSSAINI, *in* "Proceedings, 9th International Conference on Numerical Methods in Fluid Dynamics," Vol. 19, p. 6, 1984.